Enhanced O_2 flux of $CaTiO_3$-based membranes by Mn-doping

Jonathan. M. Polfus*, Wen Xing, Marit Riktor, Martin F. Sunding, Paul Inge Dahl, Sidsel M. Hanetho, Tommy, Mokkelbost, Yngve Larring, Marie-Laure Fontaine, Rune Bredesen

SINTEF Materials and Chemistry, Forskningsveien 1, NO-0314 Oslo, Norway

*Contact email: jonathan.polfus@sintef.no

Abstract

Dense symmetric membranes of $CaTi_{0.85-x}Fe_{0.15}Mn_xO_{3-\delta}$ (x=0.1, 0.15, 0.25, 0.4) are investigated in order to determine the optimal Mn-dopant content with respect to highest O_2 flux. O_2 permeation measurements are performed as function of temperature between 700-1000 °C and as function of the feed side p_{O_2} ranging between 0.01-1 bar. X-ray photoelectron spectroscopy is utilized to elucidate the charge state of Mn, and synchrotron radiation X-ray powder diffraction is employed to investigate the structure symmetry and cell volume of the perovskite phase at temperatures up to 800 °C. The highest O_2 permeability is found for x=0.25 over the whole temperature and p_{O_2}-ranges, followed by x=0.4 above 850 °C. The O_2 permeability for x=0.25 reaches 0.01 ml(STP) min^{-1} cm^{-1} at 925 °C with 0.21 bar feed side p_{O_2} and Ar sweep gas. X-ray photoelectron spectroscopy indicates that the charge state of Mn changes from approx. +3 to +4 when x>0.1, which implies that Mn mainly improves electronic conductivity for x>0.1. The cell volume is found to decrease linearly with Mn-content, which coincides with an increase in the activation energy of O_2 permeability. These results are consistent with the interpretation of the temperature and p_{O_2} dependency of O_2 permeation. The sintering behavior and thermal expansion properties are investigated by dilatometry, which show improved sinterability with increasing Mn-content and that thermal expansion coefficient decreases from 12.4 to 11.9×10^{-6} K^{-1} for x=0 and x=0.25, respectively.

1. Introduction

Oxygen separation from air is of considerable interest for implementation of CO_2 capture technologies such as oxy-fuel combustion and gasification of coal and biomass for power generation and energy demanding industries.[1,2] Dense ceramic oxygen selective membranes are furthermore of interest for use in high temperature catalytic membrane reactors for, e.g., partial oxidation of methane to synthesis gas, oxidative coupling of methane and dehydrogenation processes.[3–7] The membrane materials that exhibit the highest O_2 permeation fluxes, such as Sr/Ba and Co-containing perovskites,[8–11] suffer from poor thermodynamic and kinetic stability during operation.[9,12–14] Therefore, one approach for bringing dense ceramic O_2 permeable membranes closer to utilization in the above-mentioned application and technologies is to improve the O_2 permeability of a stable base material.

$CaTiO_3$-based perovskite oxides are cheap, non-toxic, exhibit high thermo-mechanical stability (creep) and are chemically stable in large oxygen chemical potential gradients at high temperature and CO_2 containing atmospheres.[15,16] Oxygen permeation through $CaTiO_3$ and similar oxides proceeds according to ambipolar transport of oxide ions – by means of oxygen vacancies, $v_O^{\cdot\cdot}$, in Kröger-Vink notation – and electronic charge carriers. Ambipolar conductivity is therefore facilitated by the addition of lower-valent dopants such as Fe^{3+} on the Ti-site, which according to electroneutrality will promote the concentrations of oxygen vacancies and electron holes.[17] While the total and electronic conductivity of $CaTi_{1-y}Fe_yO_{3-\delta}$ (CTF) increases with the Fe-dopant concentration, y, the oxide ion conductivity decreases

above approx. y=0.2 due to trapping of oxygen vacancies and partial transition to an ordered brownmillerite $Ca_2Fe_2O_5$.[16,18–22]

The electronic conductivity of $CaTi_{1-y}Fe_yO_{3-\delta}$ is p-type for $p_{O_2} \gtrsim 1\times10^{-5}$ bar based on reports for y=0-0.5 and temperatures up to 1200 °C.[23,24] These electrical measurements also show that the conductivity is predominately ionic over a broad p_{O_2}-range. The ambipolar conductivity and O_2 permeability may therefore be limited by p-type electronic conductivity – which is proportional to $p_{O_2}^{\frac{1}{4}}$ – particularly at the sweep side of the membrane where p_{O_2} can be quite low depending on the operating conditions. Further improvement of the O_2 permeability of the $CaTiO_3$ system therefore seems to necessitate dopants yielding increased ionic *and* electronic conductivity as well as high dopant solubility. In this respect, we recently identified Mn as a suitable dopant for increasing the O_2 permeability of the CTF system based on O_2 permeation measurements on $CaTi_{0.75}Fe_{0.15}Mn_{0.1}O_{3-\delta}$.[25] X-ray photoelectron spectroscopy and density functional theory (DFT) calculations indicated that Mn predominately exists in the +3 charge state and introduces electronic states within the band gap which may be beneficial for electronic conduction.

In the present work, we further investigate the $CaTi_{0.85-y}Fe_{0.15}Mn_xO_{3-\delta}$ system (x=0.1, 0.15, 0.25, 0.4) with respect to optimized O_2 permeability. We present O_2 flux measurements of densely sintered disc shaped membranes as function of temperature and feed side p_{O_2}. Furthermore, synchrotron radiation X-ray powder diffraction (SR-XPD) is performed as function of temperature in order to investigate variations in the crystal symmetry and cell volume with Mn content at relevant membrane operating conditions. X-ray photoelectron spectroscopy is utilized to elucidate the charge state of Mn. The sintering and thermal expansion properties are investigated in order to assess the systems compatibility with alloys and seals for module integration. Thermogravimetric analysis (TGA) is performed to elucidate the expansion of the unit cell volume as function of temperature.

2. Experimental

2.1 Synthesis, sample preparation and thermal expansion

Ceramic powders of $CaTi_{0.85-x}Fe_{0.15}Mn_xO_{3-\delta}$ (x=0, 0.1, 0.15, 0.25 and 0.4), denoted CTFMn10-40, were synthesized using nitrate salts as precursor materials, citric acid as a complexing agent and ethylene glycol for polymerization. A detailed description of the synthesis procedure is reported in Ref.[25]. Self-ignition and decomposition of the produced gels occurred upon heating to 200-250 °C and the residual powders were pre-calcined at 400 °C, gently crushed in a mortar, and annealed at 900 °C for 6 h in ambient air.

The sintering behavior of uniaxially pressed samples (∅ = 7 mm, 120 MPa) was investigated using a push-rod dilatometer (Netzsch, DIL 402E) up to approx. 1480 °C in ambient air with heating/cooling rates of 2 °C min^{-1}. Thermal expansion properties were analyzed using the same equipment on samples sintered at 1300 °C for 6 h in ambient air. O_2 flux measurements were performed on uniaxially pressed samples (∅ = 20 mm) sintered according to the same procedure. The sintered disc samples were gradually polished to a roughness of 6 µm and 1 µm with SiC grinding paper and diamond paste, respectively. The final thicknesses of the samples were 1.00, 0.88, 1.50 and 0.88 mm for CTFMn10-40.

2.2 O_2 flux measurements

The sintered disc samples were sealed to alumina support tubes (∅ = 12 mm) in a ProboStat measurement cell (NorECs, Norway) with similarly polished gold O-ring gaskets (made by welding gold wire of ∅ = 1 mm). An alumina spring load assembly provided a force of approx. 45 N on the sample against the gold gasket and alumina support tube during sealing

and measurements. Mass flow controllers were utilized to supply O_2/He feed gas mixtures and Ar sweep gas at 50 and 25 ml min^{-1}, respectively. The concentrations of O_2 permeate and He leakage were measured with a Varian CP-4900 gas chromatograph (GC). A S-type thermocouple was placed in the vicinity of the sample and gold O-ring inside the measurement cell, which was inserted into a vertical tube furnace. A gas tight seal was usually obtained by heating to 1000 °C in air, and the He leakage rate for all measurements was well below 1% of oxygen permeation. Oxygen permeation fluxes were measured at temperatures between 700-1000 °C and as function of the feed side oxygen partial pressure, $\boldsymbol{p_{O_2}}$, in the range 10^{-2} to 1 bar. The possibility of limiting surface kinetics was investigated for CTFMn25 by performing additional O_2 permeation measurements with platinum ink (Engelhard A-3788) applied to the feed and sweep side of the specimen. For dense ceramic membranes, the O_2 permeability, J_{O_2}, is taken as the thickness normalized O_2 flux at given feed and sweep side conditions with units ml(STP) min^{-1} cm^{-1}.

2.3 Synchrotron radiation X-ray powder diffraction (SR-XPD)

SR-XPD experiments were performed at beamline BM01A at the Swiss-Norwegian Beam Lines (SNBL), European synchrotron radiation facility (ESRF), Grenoble, France. The diffraction data were collected with a PILATUS 2M detector at the PILATUS@SNBL diffractometer. The wavelength and detector geometry were calibrated using a LaB_6 external standard: the wavelength was 0.70778 Å and the sample to detector distance was 343 mm. Powder samples of CTFMn10-40 were obtained from crushed sintered disc specimens, and contained in quartz capillaries (∅ = 0.5 mm). Diffraction data were collected at isotherms in steps of 10 °C in the temperature range 50 to 800 °C. The heating rate was 10 °C min^{-1} and a dwell time of 60 s and an exposure time of 30 s were used for each scan, i.e., the average heating rate was approx. 4 °C min^{-1}. The capillaries were rotated 300° during exposure to improve powder averaging. The sample temperature was calibrated using an external Ag standard. Data processing was carried out using the SNBL ToolBox,[26], and the two-dimensional data were integrated in to one-dimensional powder diffraction patterns using the Fit2D software.[27] The diffraction patterns were analyzed by Rietveld refinement using the Fullprof suite.[28]

2.4 X-ray photoelectron spectroscopy

After the O_2 permeation measurements, the CTFMn10-40 samples were equilibrated at 900 °C in a vertical tube furnace (ambient air, 19 h) and subsequently quenched by dropping them directly into liquid N_2 for retaining the oxygen non-stoichiometry and dopant charge state, as described earlier.[25] The samples were fractured under vacuum in the spectrometer in order to expose fresh surface from the bulk of the material and to avoid surface oxidation. XPS spectra were acquired on an Axis Ultra^{DLD} spectrometer (Kratos Analytical, UK) using monochromatic AlKα radiation. The employed acquisition settings allow for an energy resolution of 0.7 eV, as determined by the full width at half maximum of the Ag $3d_{5/2}$ peak of sputter cleaned silver.

2.5 Thermogravimetry

Thermogravimetrical analysis was performed on finely crushed powders of a sintered CTFMn25 pellet in synthetic air using a Netzsch STA 449C. Heating rates of 2 and 10 °C min^{-1} were used up to 1000 °C, followed by dwelling for 2 hours and cooling to room temperature at 10 °C min^{-1}. Prior to each analysis, a background curve was recorded with an empty alumina crucible.

3. Results

3.1 O_2 permeation measurements

The O_2 permeabilities CTFMn10-40 are shown as function of inverse temperature in Figure 1a. CTFMn25 exhibits the highest O_2 permeability at all temperatures followed by CTFMn40 at temperatures above 850 °C. The CTFMn40 sample, however, disintegrated upon changing the atmosphere from $\boldsymbol{p_{O_2}}$=0.21 to 0.03 bar while lowering the temperature from 800 to 775 °C at 25 °C h^{-1} ramp rate. No changes were observed in the structure of the disintegrated sample by XRD (Figure S1), and further measurements were not performed for this composition. The O_2 permeability of CTFMn15 and CTFMn10 are similar and higher than CTF.[25] Figure 1b shows an Arrhenius type plot of $J_{O_2} \cdot T$, and the corresponding activation energies from the linear fits in the two temperature regimes, E_a^1 and E_a^2, are listed in Table 1. The O_2 permeability of CTFMn25 was essentially the same with and without Pt-coating for feed side $\boldsymbol{p_{O_2}}$=0.21 at 900 °C. Considering that CTFMn25 exhibits the highest O_2 permeability, this gives an indication that the O_2 permeability is not limited by surface kinetics for these samples and experimental conditions.

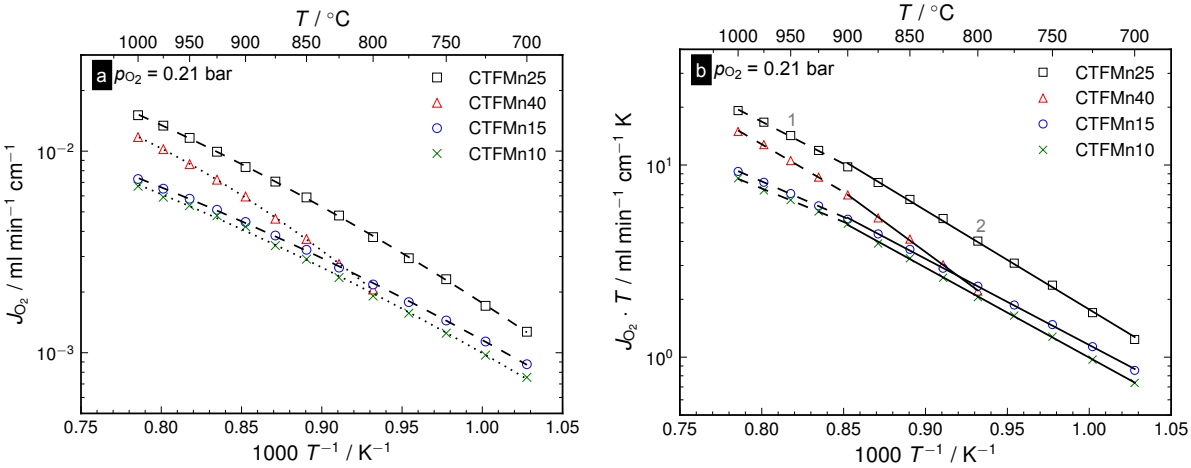

Figure 1: O_2 permeability for feed side $\boldsymbol{p_{O_2}}$=0.21 bar as function of inverse temperature (a) and Arrhenius type plot (b). The corresponding activation energies from the linear fits in (b) are listed in Table 1.

Table 1: Activation energies of O_2 permeability from linear fits in the Arrhenius type plot in Figure 1b.

Specimen	$\boldsymbol{E_a^1}$ **/ eV**	$\boldsymbol{E_a^2}$ **/ eV**
CTFMn10	0.69	0.93
CTFMn15	0.74	0.89
CTFMn25	0.87	1.02
CTFMn40	0.98	1.24

The O_2 permeability as function of feed side $\boldsymbol{p_{O_2}}$ is shown for CTFMn15-40 in Figure 2.

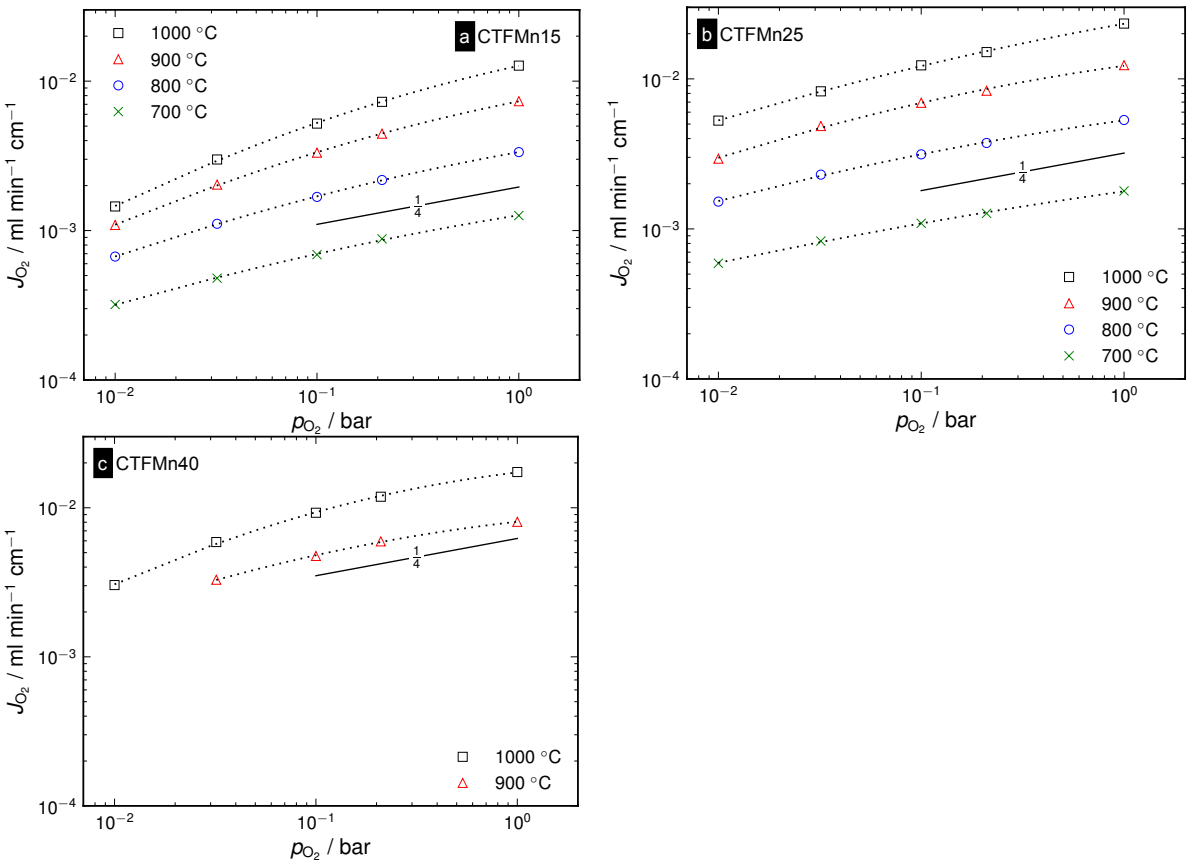

Figure 2: O_2 permeability as function of feed side $\boldsymbol{p_{O_2}}$ for CTFMn15 (a), CTFMn25 (b) and CTFMn40 (c) at 1000-700 °C. The CTFMn40 sample disintegrated as described in the text.

3.2 Synchrotron radiation X-ray powder diffraction (SR-XPD)

The $CaTiO_3$ perovskite takes the orthorombic P*bnm* space group at room temperature and transforms to the ideal cubic structure (P*m*3*m*) at high temperatures, with an intermediate tetragonal phase (I4/*mcm*).[29] Partial substitution of Ti by Fe ($CaTi_{1-y}Fe_yO_{3-\delta}$) has been found to reduce the transition temperatures, and phase transitions from orthorombic to tetragonal and cubic symmetry is reported at room temperature with increasing Fe content for $0 \leq y \leq 0.4$.[30]

Analysis of the diffraction data shows that the CTFMn10-40 samples are P*bnm* perovskites at ambient conditions. The reflections corresponding to orthorhombic distortion from the cubic structure decreases with increasing temperature, but are present in all data sets up to 802 °C. The P*bnm* space group is thus used for analysis of unit cell parameters and volume in the whole temperature range.

Figure 4 shows the cell volume as function of temperature for CTFMn10-40, and the inset shows a linear decrease in lattice volume with Mn-content at 20 and 777 °C. All samples exhibit a non-linear expansion in the 150-400 °C range, which may be attributed to oxygen uptake as measured by thermogravimetry (see section 3.5). This non-linearity is most prominent for CTFMn25 followed by CTFMn10-15 and CTFMn40. As indicated by the fits, the lattice expansion becomes linear at higher temperatures. The corresponding linear thermal expansion coefficients are 18.2×10^{-6}, 16.6×10^{-6}, 17.8×10^{-6} and 17.6×10^{-6} K^{-1} for CTFMn10-40 between 588-802 °C (777 °C for CTFMn15).

The pseudo-cubic lattice parameters as function of temperature are shown in Figure 4. Lattice parameter *b** exhibits the lowest thermal expansion in all samples, and the symmetry increases towards tetragonal as *b** approaches *c**. For CTFMn25 *b** crosses *c** just below 650

°C. CTFMn25 is thus metrically tetragonal at one temperature, but there is no phase transition associated with this feature.

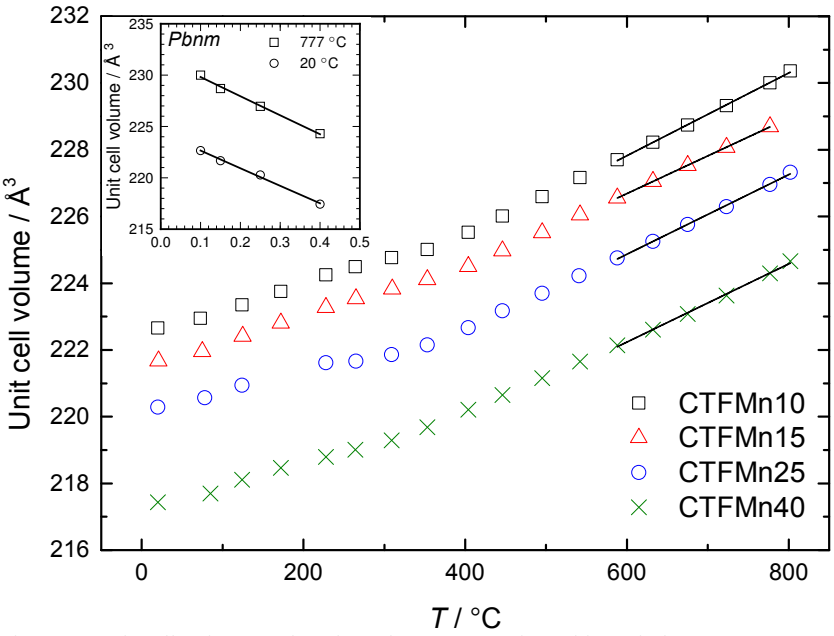

Figure 3: Unit cell volume as function of temperature in ambient air for CTFMn10-40 with linear fits for 588-802 °C (777 °C for CTFMn15). The inset shows that the relationship between Mn-content and lattice volume is linear at 20 and 777 °C.

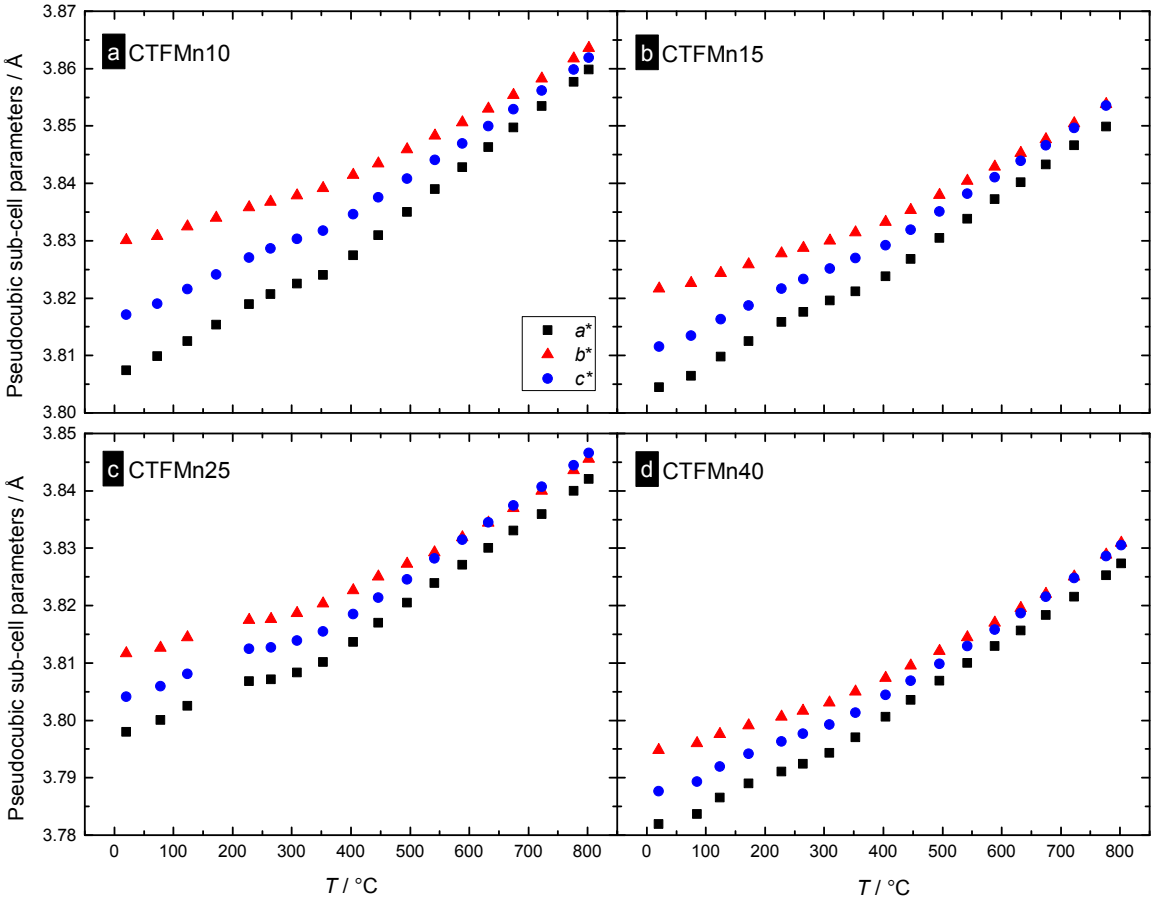

Figure 4: Pseudocubic cell parameters as function of temperature in ambient air for CTFMn10 (a), CTFMn15 (b), CTFMn25 (c) and CTFMn40 (d). The diffraction data was fitted to the *Pbnm* space-group. The pseudocubic sub-cell parameters are obtained from the *Pbnm* lattice parameters according to $a^*=\sqrt{2}a$, $b^*=\sqrt{2}b$, $c^*=2c$. One scan is missing between 150 and 200 °C for CTFMn25 due to absence of the synchrotron beam.

3.3 X-ray photoelectron spectroscopy

The Mn and Fe 2p XPS spectra show only small differences between the samples (Figure 5). The Mn 2p spectra fit well with published spectra for Mn^{+3} in Mn_2O_3.[31,32] The presence of Mn^{+4} can, however, not be excluded as differences in the bond geometry between MnO_2, characterised in the cited references, and CTFMn can lead to differences in the spectral shape. The satellite present in the Fe 2p spectra, marked with an arrow in Figure 5b, is characteristic for Fe^{3+}.[31–33] The additional presence of Fe in other oxidation states cannot be excluded as it will not show up with characteristic spectral feature but will mostly affect the satellite intensity relative to the main peak.

Manganese 3s spectra show a main peak – satellite doublet structure due to multiplet splitting. This spectral structure reflects the total spin of the atom and is thus a good measure of the oxidation state.[34] The Mn 3s XPS spectra obtained on the CTFMn samples are shown in Figure 6 together with the peak fitting results. The CTFMn10 sample differs from the other three samples by a clearly larger separation between the Mn 3s main peak and the satellite. The separation between the main peak and the satellite amounts to 5.2±0.2 eV in the CTFMn10 sample and indicates an oxidation state near +3 while the separation amounts to between 4.5 and 4.7 ±0.2 eV in the samples CTFMn15, CTFMn25 and CTFMn40 and indicates an oxidation state near +4.[31,32,35]

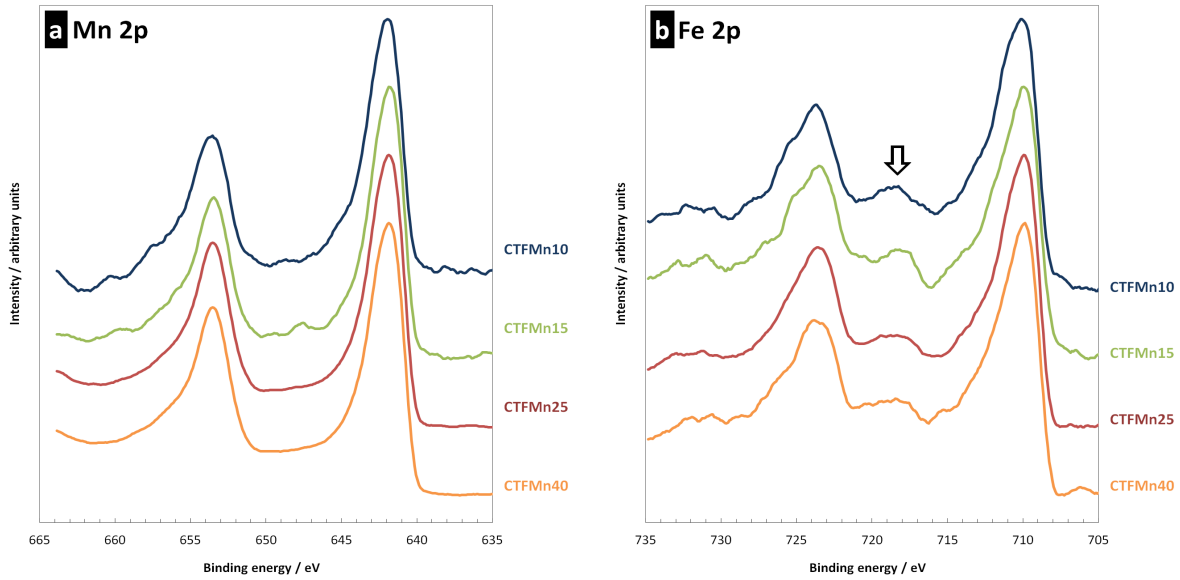

Figure 5: Mn 2p (a) and Fe 2p (b) energy region obtained by XPS on the CTFMn samples. The arrow indicates the position of the Fe $2p_{3/2}$ satellite.

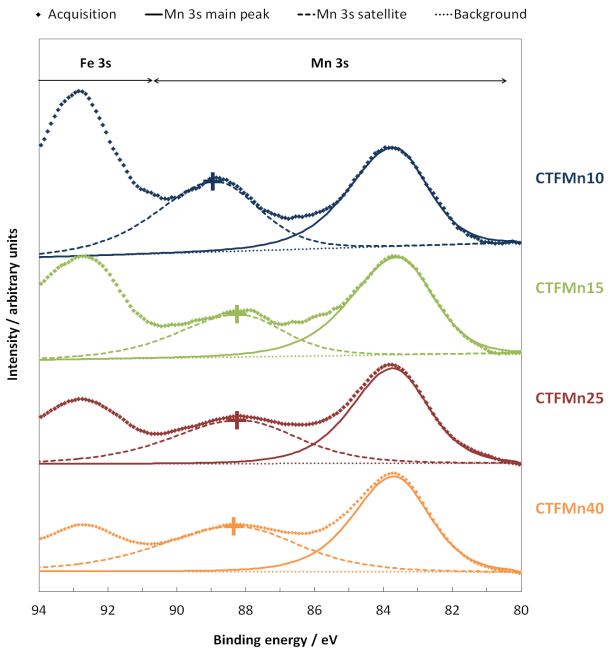

Figure 6: Mn 3s energy region obtained by XPS on CTFMn10-40 samples. The peak fitting components are indicated as well as the centre position of the satellite (cross).

3.4 Dilatometry

The sintering behavior of the CTFMn10-40 materials is presented in Figure 7. The sintering onset temperature is around 800 °C for all samples and the initial shrinkage is highest for CTF. Linear shrinkage increases with Mn-content and sintering is complete at 1250-1450 °C.

Thermal expansion coefficients (TEC) as a function of temperature for CTF, CTFMn10 and CTFMn25 are shown in Figure 8. There is a clear difference between the TEC values obtained from three adjacent temperature cycles for all 3 materials, indicating the need for annealing at high temperature to obtain equilibrium. The variations between the 3 cycles seem to increase with increasing Mn-content. While the values of TEC for the low temperature ranges (50-700 °C and lower) vary significantly for each temperature cycle, the second and third cycle provide overlapping TEC values for the high temperature ranges (50-800 °C and higher). The TEC decreases with increasing Mn-content and is 12.4, 12.2 and 11.9×10^{-6} K^{-1} for CTF, CTFMn10 and CTFMn25, respectively, in the 50-1000 °C temperature range.

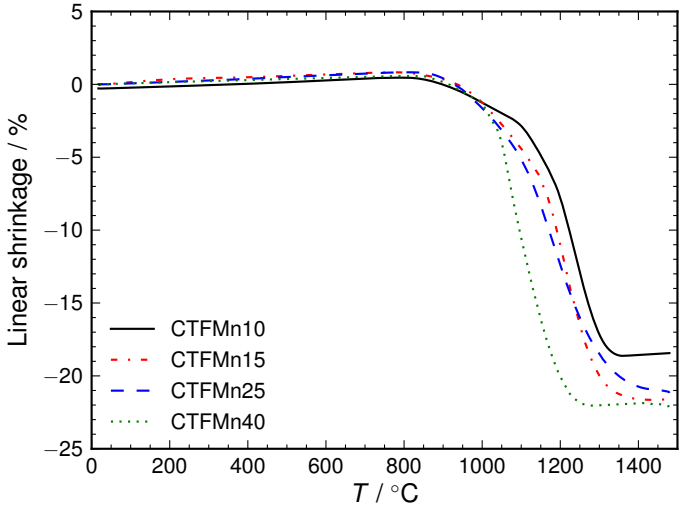

Figure 7: Linear shrinkage of CTFMn10-40 in comparison with CTF reference sample measured in ambient air.

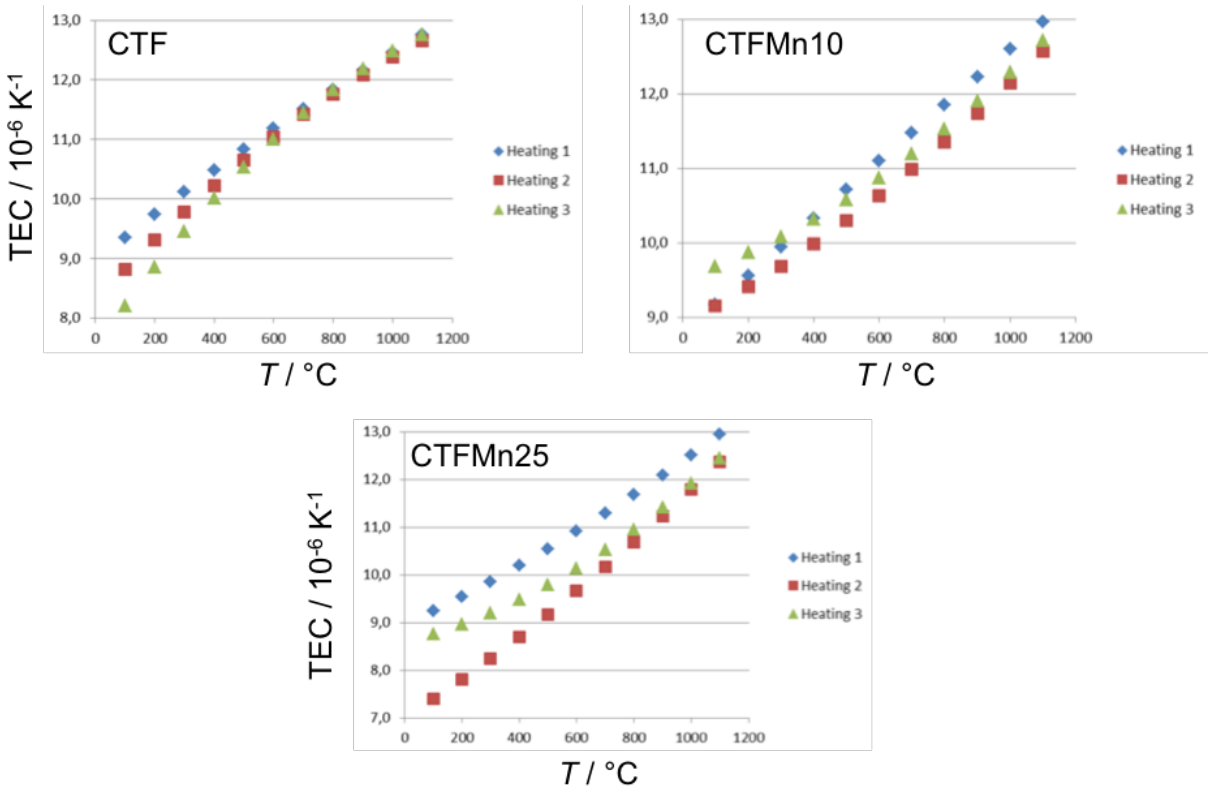

Figure 8: Thermal expansion coefficient as a function of temperature upon 3 heating cycles for CTF, CTFMn10 and CTFMn25.

3.5 Thermogravimetry

TGA was performed on CTFMn25 since it exhibited the most significant non-linear cell volume expansion with SR-XPD (see Figure 4). As shown in Figure 9, there is a pronounced weight increase during heating in the 150-450 °C temperature range. This corresponds well with the non-linear cell volume expansion observed with SR-XPD in the 150-400 °C (at an intermediate heating rate of approx. 4 °C min^{-1}) which then can be attributed to an oxidation process. The weight increase from 200-450 °C amounts to approx. 9×10^{-3} mol oxygen per mol formula unit CTFMn25. The difference between the heating and cooling curves indicate limiting redox reaction kinetics at lower temperatures.

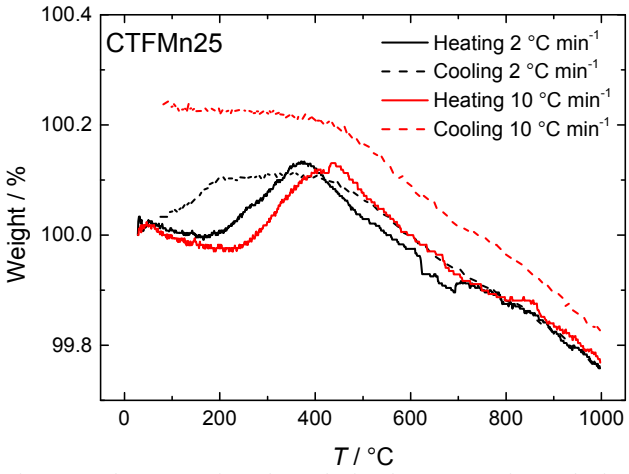

Figure 9: Thermogravimetric analysis of CTFMn25 in synthetic up to 1000 °C heating and cooling cycles at 2 and 10 °C min^{-1}.

4. Discussion

Figure 10a shows the O_2 permeability of CTFMn10-40 as function of Mn-content at 700-1000 °C and constant feed side $\boldsymbol{p_{O_2}}$=0.21 bar, as well as Mn-free CTF data from our previous work.[25] The increase in J_{O_2} with x exceeds linearity around x=0.25, indicating that the Mn dopant concentration does not simply increase the conductivity of the limiting charge carrier for O_2 permeability.

In Figure 2 the functional dependencies of J_{O_2} with feed side $\boldsymbol{p_{O_2}}$ are close to $\frac{1}{4}$ for CTFMn15 and slightly lower for CTFMn25-40. As discussed in our previous work on the same material system,[25] J_{O_2} approximately proportional to $p_{O_2}^{\frac{1}{4}}$ corresponds to limiting p-type electronic conductivity, while a lower functional dependency corresponds to ambipolar conductivity being independent of $\boldsymbol{p_{O_2}}$ and J_{O_2} follows the ratio of the oxygen pressures at the feed and permeate sides. This indicates that the O_2 permeability of CTFMn10-15 is mainly limited by p-type electronic conductivity, while that of CTFMn25-40 is mainly limited by the oxygen chemical potential gradient for higher feed side $\boldsymbol{p_{O_2}}$ (>0.01 bar).

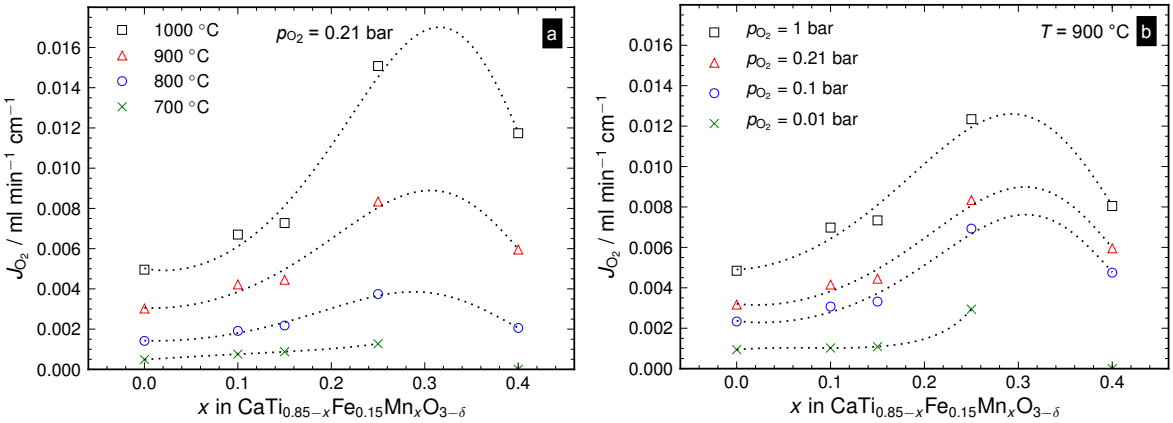

Figure 10: O_2 permeability as function of Mn content for 700-1000 °C at feed side $\boldsymbol{p_{O_2}}$=0.21 bar (a) and feed side $\boldsymbol{p_{O_2}}$ 0.01-1 bar at 900 °C. Values for x=0 are taken from Ref.[25]

The structure symmetry of CTFMn15-40 is similar in the 700-800 °C range relevant for the O_2 permeation measurements (Figure 4) which indicates that variations in oxide ion mobility associated with structure symmetry is not governing J_{O_2}. Figure 11 shows the activation energies of J_{O_2} from Figure 1b and Table 1 as function of Mn-content; the unit cell volume decreases linearly with x as shown in the inset. The activation energies of J_{O_2} correspond well with activation energies of oxide ion transport in the lower temperature range (E_a^2) with increasing influence of the generation of electronic charge carriers at higher temperatures (E_a^1).[23–25] Thus, Figure 11 indicates that the migration energy of oxide ions is closely related to the lattice volume and decreases with Mn-content. While the difference in the dependence of E_a^1 and E_a^2 on x is difficult to ascertain, a seemingly lower dependence for E_a^1 may be explained by a larger influence of electronic charge carriers which are promoted by the addition of Mn.

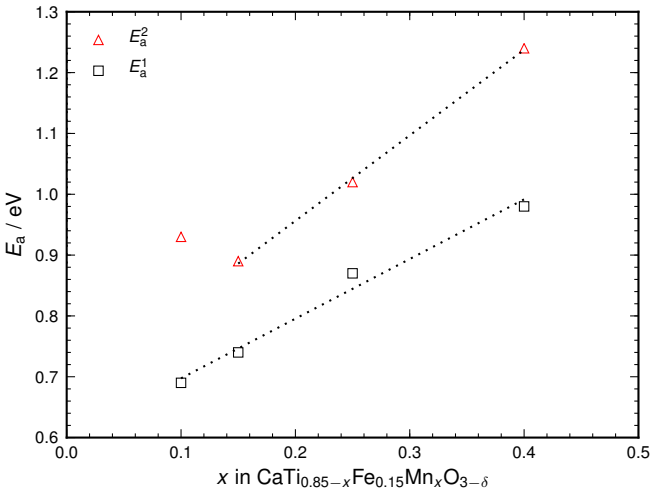

Figure 11: Activation energies of J_{O_2} as function of Mn content, with possible linear fitting.

DFT calculations corresponding to the dilute concentration limit within a fixed $CaTiO_3$ lattice volume indicate that Mn exists in the +3 oxidation state.[25] The XPS results also indicate an oxidation state of Mn close to +3 for the lowest Mn concentration (CTFMn10), and further that the oxidation state changes to approx. +4 for higher Mn-contents (Figure 6). The contraction of the lattice volume from SR-XPD (Figure 3, insert) is essentially linear towards the end member, $CaMnO_3$, with a lattice volume of 207.47 Å^3 at 302 K and nominal +4 oxidation state of Mn.[36] Thus, the lattice volumes from SR-XPD agree with a +4 oxidation state for Mn, while it is difficult to ascertain the presence of Mn^{3+} for lower Mn-contents based on lattice volume. In terms of O_2 permeation, the predominance of Mn^{4+} in CTFMn25-40, which exhibit the highest O_2 permeability, implies that Mn does not significantly enhance the concentration of oxygen vacancies. Considering that the activation energy of J_{O_2} associated with oxide ion transport increases (Figure 11), this implies that Mn increases the electronic p-type conductivity, in accordance with the interpretation of the temperature and $\boldsymbol{p_{O_2}}$ dependencies of J_{O_2} discussed earlier.

In short, with increasing Mn-content, electronic conductivity and structure symmetry – both beneficial for J_{O_2} – increase, while the activation energy of J_{O_2} increases due to lower lattice volume, which is detrimental to J_{O_2}. Accordingly, it seems that CTFMn25 is close to an optimum composition for improved J_{O_2} of the investigated materials in terms of 1) sufficient p-type conductivity, also at the lower $\boldsymbol{p_{O_2}}$ of the sweep side; 2) increasing the structure symmetry and mobility of oxide ions; and 3) not increasing the activation energy of J_{O_2} due to reduced cell volume.

The O_2 permeability of CTFMn25 at 900 °C and feed side $\boldsymbol{p_{O_2}}$=0.21 is 8.3×10^{-3} ml min^{-1} cm^{-1}, which is slightly higher than for y=0.2 (CTF20) under similar conditions, 4.0-7.0×10^{-3} ml min^{-1} cm^{-1} depending on sample thicknesses.[37,38]

The increased sintering with Mn-content may be explained by a less rigid structure as reported for $La_{0.4}Ca_{0.6}Ti_{1-x}Mn_xO_3$ when the Mn-content (x) was increased from 0.2 to 0.4.[39] The reduction in thermal expansion coefficient with increasing Mn-content is in agreement with the observed structural changes with reduced pseudocubic sub-cell parameters and corresponding cell volume. Comparable results from the literature are scarce, however, the TEC for CTF ($CaTi_{0.85}Fe_{0.15}O_{3-\delta}$), 12.4×10^{-1} K^{-1}, is in agreement with reported values for $CaTi_{0.85}Fe_{0.10}O_{3-\delta}$, which are in the range of 10.6 to 14.5×10^{-1} K^{-1},[40] and measured by the same procedure (3 temperature cycles) by Paulsen to 12.7×10^{-1} K^{-1}.[41]

5. Conclusions

The O_2 permeability of $CaTi_{0.85-y}Fe_{0.15}Mn_xO_{3-\delta}$ (x=0.1, 0.15, 0.25, 0.4) is found to be highest for x=0.25, reaching 0.01 ml min^{-1} cm^{-1} at 925 °C with 0.21 bar feed side p_{O_2} and Ar sweep gas. The activation energy of O_2 permeability – mainly associated with the migration enthalpy of oxide ions – increases with Mn-content and corresponds with a linear decrease of the cell volume measured by in-situ SR-PXD. The O_2 permeation measurements are furthermore interpreted in terms of limiting p-type electronic conductivity, which increases with Mn-content. These effects contribute oppositely to the O_2 permeability and a maximum is found for x=0.25. These interpretations are consistent with the charge state of Mn which by XPS is indicated to change from +3 to +4 when x>0.1, implying that Mn mainly improves electronic conductivity for x>0.1. The sinterability of the materials improves with increasing Mn content, and the TEC decreases from 12.4 to 11.9×10^{-1} K^{-1} for CTF and CTFMn25, respectively.

6. Acknowledgements

This research has received funding from the European Union Seventh Framework Programme (FP7/2007-2013) via grant agreement no. FP7-ENERGY-268165, “Highly Efficient Tubular Membranes for Oxy-Combustion” (HETMOC).

7. References

1. IEA, *Technology Roadmap: Carbon capture and storage*, 2013.

2. S. S. Hashim, a. R. Mohamed, and S. Bhatia, *Renew. Sustain. Energy Rev.*, 2011, **15**, 1284–1293.

3. H. J. M. Bouwmeester, *Catal. Today*, 2003, **82**, 141–150.

4. A. Thursfield and I. S. Metcalfe, *J. Mater. Chem.*, 2004, **14**, 2475.

5. M. Rebeilleau-Dassonneville, S. Rosini, A. C. van Veen, D. Farrusseng, and C. Mirodatos, *Catal. Today*, 2005, **104**, 131–137.

6. W. Yang, H. Wang, X. Zhu, and L. Lin, *Top. Catal.*, 2005, **35**, 155–167.

7. J. Sunarso, S. Baumann, J. M. Serra, W. A. Meulenberg, S. Liu, Y. S. Lin, and J. C. Diniz da Costa, *J. Memb. Sci.*, 2008, **320**, 13–41.

8. Y. Teraoka, H.-M. Zhuang, S. Furukawa, and N. Yamazoe, *Chem. Lett.*, 1743–1746.

9. Z. Shao, W. Yang, Y. Cong, H. Dong, J. Tong, and G. Xiong, *J. Memb. Sci.*, 2000, **172**, 177–188.

10. J. Tong, W. Yang, R. Cai, B. Zhu, G. Xiong, and L. Lin, *Sep. Purif. Technol.*, 2003, **32**, 289–299.

11. S. Baumann, J. M. Serra, M. P. Lobera, S. Escolástico, F. Schulze-Küppers, and W. a. Meulenberg, *J. Memb. Sci.*, 2011, **377**, 198–205.

12. L. Qiu, T. H. Lee, L.-M. Liu, Y. L. Yang, and A. J. Jacobsen, *Solid State Ionics*, 1995, **76**, 321–329.

13. A. Thursfield and I. S. Metcalfe, *J. Memb. Sci.*, 2007, **288**, 175–187.

14. H. Lein, K. Wiik, and T. Grande, *Solid State Ionics*, 2006, **177**, 1587–1590.

15. T. Esaka, T. Fujii, K. Suwa, and H. Iwahara, *Solid State Ionics*, 1990, **40-41**, 544–547.

16. F. Figueiredo and M. Soares, *J. Electroceramics*, 2004, 627–636.

17. H. Iwahara, T. Esaka, and T. Mangahara, *J. Appl. Electrochem.*, 1988, **18**, 173–177.

18. E. Chinarro, *Solid State Ionics*, 2003, **160**, 161–168.

19. A. I. Becerro, C. McCammon, F. Langenhorst, F. Seifert, and R. Angel, *Phase Transitions*, 1999, **69**, 133–146.

20. A. Becerro, F. Seifert, and R. Angel, *J. Phys. Condens. Matter*, 2000, **12**, 3661–3670.

21. C. McCammon, A. I. Becerro, F. Langenhorst, R. J. Angel, S. Marion, and F. Seifert, *J. Phys. Condens. Matter*, 2000, **12**.

22. F. M. Figueiredo, J. Waerenborgh, V. V Kharton, H. Na, and J. R. Frade, *Solid State Ionics*, 2003, **156**, 371–381.

23. S. Marion, A. I. Becerro, and T. Norby, *Ionics (Kiel).*, 1999, **5**, 385–392.

24. L. Dunyushkina and V. Gorbunov, *Ionics (Kiel).*, 2002, **8**, 256–261.

25. J. M. Polfus, W. Xing, S. M. Hanetho, M. F. Sunding, P. I. Dahl, Y. Larring, M. Fontaine, and R. Bredesen, *to be Submitt.*, 2014.

26. V. A. Dyadkin, *SNBL ToolBox, Swiss-Norwegian Beam Lines at ESRF, Grenoble, France*, 2012.

27. A. P. Hammersley, S. O. Svensson, M. Hanfland, A. N. Fitch, and D. Hausermann, *High Press. Res.*, 1996, **14**, 235–248.

28. J. Rodriguez-Carvajal, *LLB Sacley LCSIM Rennes. Fr.*, 2003.

29. S. A. T. Redfern, *J. Phys. Condens. Matter*, 1996, **8**, 8267–8275.

30. A. I. Becerro, S. A. T. Redfern, M. A. Carpenter, K. S. Knight, and F. Seifert, *J. Solid State Chem.*, 2002, **167**, 459–471.

31. P. A. W. van der Heide, *J. Electron Spectros. Relat. Phenomena*, 2008, **164**, 8–18.

32. M. C. Biesinger, B. P. Payne, A. P. Grosvenor, L. W. M. Lau, A. R. Gerson, and R. S. C. Smart, *Appl. Surf. Sci.*, 2011, **257**, 2717–2730.

33. A. Bocquet, A. Fujimori, T. Mizokawa, T. Saitoh, H. Namatame, S. Suga, N. Kimizuka, Y. Takeda, and M. Takano, *Phys. Rev. B*, 1992, **45**, 1561–1570.

34. D. Briggs, in *Surface Analysis by Auger and X-Ray Photoelectron Spectroscopy*, eds. D. Briggs and J. T. Grant, IM Publications, 2003, vol. 1, pp. 31–56.

35. V. Di Castro and G. Polzonetti, *J. Electron Spectros. Relat. Phenomena*, 1989, **48**, 117–123.

36. W. Paszkowicz, J. Piętosa, S. M. Woodley, P. A. Dłużewski, M. Kozłowski, and C. Martin, *Powder Diffr.*, 2012, **25**, 46–59.

37. F. . Figueiredo, V. . Kharton, a. . Viskup, and J. . Frade, *J. Memb. Sci.*, 2004, **236**, 73–80.

38. A. L. Shaula, R. O. Fuentes, F. M. Figueiredo, V. V. Kharton, F. M. B. Marques, and J. R. Frade, *J. Eur. Ceram. Soc.*, 2005, **25**, 2613–2616.

39. N. Raeis Hosseini, N. M. Sammes, and J. S. Chung, *J. Power Sources*, 2014, **245**, 599–608.

40. A. A. Murashkina, A. N. Demina, A. K. Demin, V. I. Maragou, and P. E. Tsiakaras, *Solid State Ionics*, 2008, **179**, 1615–1619.

41. O. Paulsen, Norges teknisk-naturvitenskapelige universitet, Trondheim (Norway), 2009.